Published in final edited form as:

IEEE Trans Med Imaging. 2022 September ; 41(9): 2399–2413. doi:10.1109/TMI.2022.3164568.

Design Optimization of Spatial-Spectral Filters for Cone-Beam CT Material Decomposition

Matthew Tivnan [Student Member, IEEE],
Johns Hopkins University, Department of Biomedical Engineering, Baltimore, MD 21218

Wenying Wang,
Johns Hopkins University, Department of Biomedical Engineering, Baltimore, MD 21218

Grace Gang,
Johns Hopkins University, Department of Biomedical Engineering, Baltimore, MD 21218

J. Webster Stayman [Senior Member, IEEE]
Johns Hopkins University, Department of Biomedical Engineering, Baltimore, MD 21218

Abstract

Spectral CT has shown promise for high-sensitivity quantitative imaging and material decomposition. This work presents a new device called a spatial-spectral filter (SSF) which consists of a tiled array of filter materials positioned near the x-ray source that is used to modulate the spectral shape of the x-ray beam. The filter is moved to obtain projection data that is sparse in each spectral channel. To process this sparse data, we employ a one-step direct model-based material decomposition (MBMD) to reconstruct basis material density images directly from the SSF CT data. To evaluate different possible SSF designs, we define a new Fisher-information-based predictive image quality metric called separability index which characterizes the ability of a spectral CT system to distinguish between the signals from two or more materials. This spectral CT performance metric can be used to optimize spectral CT system design. We conducted simulation-based design optimization study to find optimized combinations of filter materials, filter thicknesses, filter widths, and source settings. Finally, we present MBMD results using simulated SSF CT measurements from the optimized designs to demonstrate the ability to reconstruct basis material density images and to show the benefits of the optimized designs. Our results indicate that optimizing SSF CT for separability leads to high-performance at material discrimination tasks.

Index Terms—

Cone-Beam CT; Design Optimization; Material Decomposition; Multi-Energy CT; K-Edge Filters; Spectral CT

mtivnan2@jhu.edu .

I. Introduction

Material discrimination is an important goal for the next generation of x-ray computed tomography (CT) systems. Different materials have different photon-energy-dependent attenuation spectra. It is, therefore, possible to collect information about material composition of an object through the incorporation of multiple measurement sensitivity spectra into one imaging system which we refer to as spectral CT. Even if two objects map to the same overall attenuation (as measured by Hounsfield units in conventional CT) they can be distinguished by the relative response across multiple spectral channels on a spectral CT system. Furthermore, if a finite number of basis materials can be assumed, the material densities can be estimated directly via a material decomposition algorithm. The material separability of a spectral CT imaging system refers to its ability to gather information which is relevant to the discrimination of two or more materials. This is related to the system spectral sensitivity which depends on the source, filter, patient attenuation, and detector spectra. In this work, we give a formal definition of material separability index, including its relationship to system spectral sensitivity, and we demonstrate how it can be used to optimize spectral CT system design.

Material density estimation from spectral CT data is an active area of research which moves CT into the domain of true quantitative imaging [1]. Recent years have seen an explosion of medical image post-processing such as anatomical segmentation, the extraction of radiomic features and computer-automated diagnosis [2]. These image processing software tools often implicitly assume that the input images represent the same physical quantity with the same units. However, it is well known that Hounsfield units vary based on the source settings, detector properties and other factors. Therefore, there is a need for standardization of the physical meaning of the numeric values which make up CT images regardless of the imaging hardware or data processing software used to generate them. Material density images serve this purpose because they have a clear physical meaning that can provide a unified quantitative basis across various systems.

Spectral CT and material density estimation also enable imaging studies that would not have been possible with conventional CT. For example, decomposition into water and calcium allows for quantitative measures of bone density. Decomposition of iodine contrast agent, enables virtual non-contrast imaging without the need for a digital subtraction step. Three or more spectral sensitivity channels would enable multi-contrast-enhanced imaging studies. For example, protocols have already been developed for multiphasic liver imaging using two different contrast agents (e.g. iodine and gadolinium) with time-delayed injections to acquire the arterial enhancement phase, venous enhancement phase, and non-contrast phase in a single acquisition [3].

Spectral CT encompasses a class of technologies which modulate the x-ray energy sensitivity spectra used to sample the energy-dependent attenuation properties of the patient. One strategy is to incorporate varied spectral sensitivities using energy-sensitive detectors. Some existing dual-energy CT systems are enabled by dual-layer detectors [4], where the low-energy photons are preferentially absorbed in the first layer, which corresponds to the low-energy channel. The high-energy channel is the second layer which interacts with

photons which have passed through the first layer. Novel photon-counting detectors are promising for the future of spectral CT because they have the ability to directly discriminate the energy of detected photons [5]. However, currently the vast majority of existing CT systems use conventional energy-integrating detectors. Some spectral CT technologies are compatible with energy-integrating detectors and are therefore candidates for incremental modification of existing imaging systems. These include dual-source CT [6], where there are two physical sources, each tuned to a different peak tube voltage as well as kV-switching [7] strategies where there the source settings are varied as a function of view angle.

Another strategy for spectral CT with energy integrating detectors is to modulate the spectrum of the incident x-ray beam using filtration materials, particularly those with a K-edges at useful energy levels. Split-filter designs have been implemented using materials such as tin or gold positioned near the source to filter a portion of the beam that covers half of the fan angles [8] or cone angles [9]. Other strategies have involved the use of spectral modulators with a repeated pattern of metal filters and gaps [10]. For a circular source trajectory, one can take advantage of the data redundancy of 360 degree acquisitions to produce two complete CT datasets with two different spectral sensitivities from one acquisition.

In this paper, we present a novel spectral modulator called a spatial-spectral filter (SSF) which uses tiled source-side filters to enable an arbitrary number of spectral channels. These filters present possible advantages in designing varied and customized spectral permitting optimization of spectral sensitivity for specific tasks. Design of these filters presents both flexibility and challenges due to the trade-off between spatial and spectral sampling.

There are many possible filter layouts, but in general, a particular spectral channel associated with one filter material is sparse and does not constitute a complete CT dataset in terms of spatial sampling of the projection domain. Therefore, alongside our presentation of this new device, we provide the data processing strategies needed to perform spatial reconstruction and material decomposition to estimate material density images directly from sparse spectral CT data acquired with a SSF.

To consider optimal designs under different situations, we introduce a new predictive image quality metric called separability index which characterizes the ability of a spectral CT system to distinguish between the signals from two or more materials. This metric is related to the Fisher information matrix and is intended to quantify the advantage a spectral CT system would have in discriminating stimuli over a traditional single-energy CT device.

In previous preliminary studies, we have demonstrated that full material decomposition is possible using SSF CT data despite the sparsity of each channel in the projection domain [11]. We have also presented preliminary results characterizing the impact of various design parameters on the material density image quality [12] [13] and implemented an initial protoype design [14]. In this work, a detailed physical description of the SSF is presented including an enumeration of the tuneable design parameters. We provide an advanced physical model for polyenergetic x-ray sources, filtration, attenuation, and detection, including models for non-ideal effects such as spectral blur and quantum noise.

An iterative model-based material decomposition algorithm is also introduced including regularization strategies to allow for spatial reconstruction from incomplete CT data. In conjunction with the new separability metric, optimized designs are sought for different imaging conditions. Finally, simulation studies are conducted for a variety of SSF designs to demonstrate improved performance for designs that have been optimized for material separability.

II. Methods

A. Spatial Spectral Filters

The beam from a conventional x-ray tube consists of x-ray photons with varied energies less than or equal to the source voltage times the charge of an electron. This spectrum is distributed according to idealized bremsstrahlung with additional filtration from the tungsten anode and other source components in the path of the beam. The proposed device is a patterned filter positioned between the x-ray source and the patient. The filter consists of a tiled array different materials (e.g., metallic foils). The polyenergetic beam from the source is incident on the filter. X-ray photons are attenuated according to the unique energy-dependent attenuation associated with the filter material it passes through at each position. Different paths of x-ray propagation (i.e., rays) will intersect different parts of the tiled filter and therefore be filtered by different materials. In this way, the ordinarily spatially uniform polyenergetic incident beam is divided into spectrally varied beamlets. The SSF modulates the spatial-spectral distribution of photons incident on the patient and consequently, the spatially-dependent sensitivity spectra of the lines of projection measured by a detector on the opposite side of the patient. A diagram showing the SSF is provided in Figure 1.

The materials and thicknesses and spatial distribution of the filters can be chosen to produce the desired shape of the sensitivity spectra. One important design consideration for metallic filters is the position of the K-edge. As a general trend, materials tend to attenuate low-energy photons at a greater rate than high-energy photons. However, there are discrete positive jumps in attenuation at the K-shell energy for a given element since another quantized level of photoelectric absorption is available to photons above this energy level. Some materials have a K-edge in the diagnostic energy range which can be very useful. For example, tin (atomic number 50) has a K-edge 29.20 keV and bismuth (atomic number 84) has a K-edge at 90.53 keV. Materials with an atomic number greater than 84, and a corresponding higher K-shell energy, are typically unstable, radioactive, or toxic. Using varied K-edge materials leads to a more diverse set of sensitivity spectra. Spectral diversity is an important consideration for separability in joint material decomposition and spatial reconstruction problems. An example of a SSF using materials (Sn, Er, Lu, Au, Pb) with K-shell energies in the diagnostic range is shown in Figure 1.

To improve the spatial-spectral sampling pattern, the SSF position must be translated as a function of view angle. For example, if the SSF is not translated, then the portion of an object positioned at the axis of rotation will only be sampled by one spectrum. This is generally not sufficient for material decomposition. There are many SSF system design parameters which control spatial-spectral sampling. In this work, we constrain the SSF to a repeating 1-dimensional array of rectangular filter tiles as shown in Figure 1. Within these

constraints, the remaining design parameters which control the static physical design of the SSF include:

1. the thickness of the filter tiles
2. the period/length of the repeating pattern of filter tiles
3. the number of filter tiles per period
4. the material of each filter tile
5. the ordering of materials in the repeating pattern
6. the relative width of each filter tile (must sum to length period)

Additionally, there are some parameters which do not pertain to the construction of the SSF. These have an effect on the system spatial-spectral sensitivity and sampling but can be adjusted between or during scans. These adjustable design parameters for SSF CT include:

1. the trajectory of the SSF translation
2. the trajectory of the source and detector
3. the distances between the source, the SSF, the object, and the detector
4. the x-ray tube voltage
5. the x-ray tube current

Adjusting these parameters allows SSF to be tuned for a wide range of possible applications. By controlling the trajectory of the SSF, we can control which parts of the object are sampled by each sensitivity spectra. The x-ray tube current and voltage can also be modulated for further control over the number and spectral distribution of photons incident on the patient. In this work we focus on optimization of the intrinsic filter parameters except for ordering, which was previously found not to be a significant factor [12]. Similarly, the CT system design was fixed with a circular cone-beam orbit and geometry; while controllable factors like tube voltage are optimized.

As compared to some other spectral CT technologies, the data collected using SSFs is incomplete in that it cannot be divided into a full CT dataset for each spectral “channel”. That is, if each filter material is considered as a separate spectral channel, then there is a sparse non-overlapping CT projection-domain dataset collected for each channel. Importantly, the spatial sampling geometry is still complete if all spectral channels are taken together. Further, if each part of the object is exposed to a different sensitivity spectra as a function of view, we have spectral information that can be used for material decomposition. Such strategies involving trade-offs between spatial and spectral sampling have been widely explored in other imaging systems (e.g. spectral imaging from air- and space-borne cameras [15].)

In the next section we present advanced data processing strategies to handle this data and strategies for optimizing the design. This includes a statistical estimation algorithm for jointly solving the spatial reconstruction and material decomposition problems as well as regularization schemes to handle the sparse spatial-spectral sampling. Moreover, a new

performance metric of material separability is introduced to quantitatively predict and select optimized filter designs.

B. Physical Models and Material Decomposition

In this section, we introduce a physical model for polyenergetic x-ray transmission and detection in spectral CT data acquisitions which can be used to model SSF CT systems.

1) Spectral CT Measurement Model: Given a multi-material density image, $\mathbf{x}$ (all voxels and materials represented as a single column vector), a discretized spectral CT measurement model, $\bar{\mathbf{y}}(\mathrm{x})$, may be written as

$$\bar{\mathbf{y}}(\mathbf{x}) = \mathbf{S}\exp(-\mathbf{QAx}) \tag{1}$$

where $\mathbf{A}$ is a forward-projection matrix operator which models line integrals, $\mathbf{Q}$ contains the mass attenuation coefficients for each basis material, and $\mathbf{S}$ is the projection- and energy-dependent spectral sensitivity. This matrix formulation has previously been used in [16] for model-based material decomposition but also represents the same basic form as models used in [17]. The shapes of these matrix operators is given in Table II-B.2.

Note, that $\mathbf{A}$ is block-diagonal across basis materials (requiring one forward projection per material) and $\mathbf{Q}$ is block-diagonal across projections. However, the system spectral sensitivity $\mathbf{S}$ can depend on both photon energy, projection, and view angle, as is the case for SSF CT which modulates the spatial-spectral 0sampling distribution differently for each projection and view.

2) Noise Model: This work focuses on indirect energy-integrating detectors, and so we expand $\mathbf{S}$ as follows:

$$\bar{\mathbf{y}}(\mathbf{x}) = \mathbf{G}_4\mathbf{B}_3\mathbf{S}_2\mathbf{S}_1\mathbf{S}_0\exp(-\mathbf{QAx}) \tag{2}$$

where the numerical subscripts loosely follow the stages of the signal and noise transfer models for detectors as presented in [18]. The operator $\mathbf{S}_0$ models the energy-dependent mean number of incident x-ray photons (after SSF filtration) for each line of response, $\mathbf{S}_1$ models the energy-dependent probability of interaction with the scintillator, $\mathbf{S}_2$ models the energy-dependent conversion to secondary quanta (optical photons) in the scintillator, $\mathbf{B}_3$ is a scintillator blur model, and $\mathbf{G}_4$ is a diagonal scaling operator used to capture optical coupling and other overall gain effects.

We assume that photons generated by the x-ray source for each energy level are Poisson-distributed and uncorrelated. Further, we assume that pre-filtration by the SSF, absorption by the patient, and scintillator interaction are binomial selection processes, so the quantity $\mathbf{S}_1\mathbf{S}_0\exp(-\mathbf{QAx})$, which represents x-ray photons which are detected, is also Poisson distributed and uncorrelated (because $\mathbf{S}_1$ is typically block diagonal across projections). However, we model $\mathbf{S}_2$, $\mathbf{B}_3$, and $\mathbf{G}_4$ as deterministic operators, so when approximating the data covariance for a given object, $\mathbf{x}$, we use the expression below.

$$\mathbf{\Sigma_y} = \mathbf{G}_4\mathbf{B}_3\mathbf{S_2}D\{\mathbf{S}_1\mathbf{S}_0\exp(-\mathbf{QAx})\}\mathbf{S}_2^T\mathbf{B}_3^T\mathbf{G}_4^T \tag{3}$$

3) Model-Based Material Decomposition: There are several possible approaches to MBMD which have the ability estimate the material density images directly from spectral CT data [19] [17]. We use the SPS algorithm described in [16] which minimizes the following penalized least-squares objective function:

$$\Phi(\mathbf{x}, \mathbf{y}) = (\mathbf{y} - \bar{\mathbf{y}}(\mathbf{x}))^T\mathbf{\Sigma_y^{-1}}(\mathbf{y} - \bar{\mathbf{y}}(\mathbf{x})) + \mathbf{x}^T\mathbf{R}\mathbf{x} \tag{4}$$

$$\hat{\mathbf{x}}(\mathbf{y}) = \underset{\mathbf{x}}{\operatorname{argmin}}\,\Phi(\mathbf{x}, \mathbf{y})\,. \tag{5}$$

The first term in (4) is the data fidelity term and the second is a cross-material quadratic roughness penalty which has been previously presented [20]. That quadratic penalty is a refinement of the familiar pairwise quadratic penalty between neighboring voxel differences, except that an additional pairwise penalty between material type is applied.

4) Normalization of Attenuated Energy: For fair comparisons between various system designs, it is often necessary to normalize the energy attenuated in the patient using the following formula.

$$E_p = \left(1.602 \times 10^{-13}\frac{\text{mJ}}{\text{keV}}\right)\boldsymbol{\varepsilon}^T\mathbf{S}_0(\mathbf{1} - \exp(-\mathbf{QAx})) \tag{6}$$

where $\mathbf{S}_0(\mathbf{1} - \exp(-\mathbf{QAx}))$ are the x-ray photons attenuated by the patient, and $\boldsymbol{\varepsilon}$ are the energies in keV of those photons. The dose in mGy is equal to this attenuated energy divided by the patient mass. This presumes that the attenuated energy is equal to the energy of all attenuated x-ray photons ignoring scattered photons that may leave the patient.

5) Modeling Spatial-Spectral Filters: Beam filtration by the SSF occurs on the source side, so it is modeled in the $\mathbf{S}_0$ term. This is beneficial as compared to detector-side filtration because the photons absorbed in the filter for the purpose of spectral shaping never actually reach the patient and therefore do not contribute to dose. The spectral modulation from an SSF is given by the following formula:

$$\mathbf{S}_0 = D\{\exp(-\mathbf{Q}_{\text{SSF}}\mathbf{B}_{\text{SSF}}\mathbf{A}_{\text{SSF}}\mathbf{x}_{\text{SSF}})\}D\{\mathbf{s}_0\}\,. \tag{7}$$

Here, $\mathbf{s}_0$ is the number of photons generated by the source at each energy before filtration, $\mathbf{x}_{\text{SSF}}$ is a voxelized multi-material model of the SSF, $\mathbf{B}_{\text{SSF}}$ is a blur model for spectral mixing effects at beamlet boundaries (due to an extended focal spot), $\mathbf{A}_{\text{SSF}}$ is the system geometry, and $\mathbf{Q}_{\text{SSF}}$ contains the mass attenuation spectra for filter materials. The SSF model voxel spacing is a configurable parameter, but should be chosen with high enough

resolution to capture spectral mixing effects at the interface between filter tiles as shown in Figure 2.

Design parameters that control the physical construction of the filter are modeled in $\mathbf{x}_{SSF}$. This includes the filter thickness, potential gaps between filter tiles, and filter tile width among other parameters. All parameters related to the system geometry and sampling, including the source-to-filter distance, source-to-axis distance, source-to-detector distance, and filter motion trajectories are modeled in $\mathbf{A}_{SSF}$. Blur due to an extended focal spot is in $\mathbf{B}_{SSF}$. Before the $\mathbf{B}_{SSF}$ operation, the beamlets are perfectly formed with sharp edges associated with a point source and after the operation the beamlets are blurred (thus spectrally mixed) to model the spectral mixing effects of an extended focal spot.

In other work [11], we have presented evidence that faster filter motion trajectories and narrower filter tile widths lead to a greater degree of uniformity in the spatial-spectral sampling pattern. We have also constructed a physical prototype and advanced data correction procedures (including spectral effects of gaps between filters) to demonstrate this device can be used for CT material decomposition with energy-integrating detectors [21]. This work focuses on physical simulation as a method to optimize the design of SSF or other spectral CT systems.

C. Performance Metrics for Multi-Material Imaging

In the following sections, we will make comparisons between varied spectral CT system designs including various SSF configurations. To make quantitative comparisons between those systems, we must define some relevant multi-material image quality metrics. In particular, we introduce a new metric of material separability. To this end, we define local approximations of the transfer function and noise for the spectral data acquisition and reconstruction.

1) Transfer Function: We begin with the assumption that the relationship between the estimated material density images, $\hat{\mathbf{x}}$ and the ground truth, $\mathbf{x}$, is approximately linear for small changes to the ground truth as shown in the expression below:

$$\boldsymbol{\Delta}\hat{\mathbf{x}} = \left[\frac{\partial \hat{\mathbf{x}}}{\partial \mathbf{x}}\right]\boldsymbol{\Delta}\mathbf{x} = \left[\frac{\partial \hat{\mathbf{x}}}{\partial \bar{\mathbf{y}}}\right]\left[\frac{\partial \bar{\mathbf{y}}}{\partial \mathbf{x}}\right]\boldsymbol{\Delta}\mathbf{x} \tag{8}$$

Here we are using the following notation for the Jacobian matrix between two vectors

$$\left[\frac{\partial \mathbf{u}}{\partial \mathbf{v}}\right]_{i,j} = \frac{\partial u_i}{\partial v_j}. \tag{9}$$

The Jacobian matrix relating the measurement model, $\bar{\mathbf{y}}$, to the ground truth, $\mathbf{x}$ is

$$\left[\frac{\partial \bar{\mathbf{y}}}{\partial \mathbf{x}}\right] = -\mathrm{SD}_{\mathbf{x}}\mathrm{QA} \tag{10}$$

where $\mathbf{D}_{\mathbf{x}} = D\{\exp(-\mathbf{QAx})\}$ are diagonal weights that depend on the object $\mathbf{x}$.

Following the differentiation method described in [22],

$$\left[\frac{\partial \hat{\mathbf{x}}}{\partial \overline{\mathbf{y}}}\right] = -\left[\frac{\partial^2 \Phi}{\partial \mathbf{x}^2}\right]^{-1}\left[\frac{\partial^2 \Phi}{\partial \mathbf{x}\,\partial \overline{\mathbf{y}}}\right] \tag{11}$$

$$\left[\frac{\partial \hat{\mathbf{x}}}{\partial \overline{\mathbf{y}}}\right] = -[\mathbf{F}+\mathbf{R}]^{-1}\left[\mathbf{A}^T\mathbf{Q}^T{\mathbf{D}_\mathbf{x}}^T\mathbf{S}^T\boldsymbol{\Sigma}_\mathbf{y}^{-1}\right] \tag{12}$$

$$\mathbf{F} = \mathbf{A}^T\mathbf{Q}^T{\mathbf{D}_\mathbf{x}}^T\mathbf{S}^T\boldsymbol{\Sigma}_\mathbf{y}^{-1}\mathbf{S}\mathbf{D}_\mathbf{x}\mathbf{Q}\mathbf{A} \tag{13}$$

where **F** is the Fisher information matrix. This is the Hessian of the objective function data fidelity term. It describes the precision (inverse of covariance) of the multi-material estimates based on the noise properties of measured data. Because the estimates include multiple materials, **F** contains information about cross-material as well as cross-voxel relationships between different estimates.

As described in [23], we can combine (10) and (12) to arrive the following expression for a local transfer function

$$\left[\frac{\partial \hat{\mathbf{x}}}{\partial \mathbf{x}}\right] = \left[\frac{\partial \hat{\mathbf{x}}}{\partial \overline{\mathbf{y}}}\right]\left[\frac{\partial \overline{\mathbf{y}}}{\partial \mathbf{x}}\right] = [\mathbf{F}+\mathbf{R}]^{-1}\mathbf{F} \tag{14}$$

Here we can see that the transfer function depends on the relationship between the Fisher information, **F**, and the regularization, **R**. This expression characterizes the spatial blur (e.g. local impulse response) as well as the cross-talk between materials. These biases are introduced and controlled by the regularization term in order to reduce noise.

2) Covariance: Approximations for the covariance including cross-material correlations was defined in [20] as follows

$$\Sigma_\mathbf{x} = \left[\frac{\partial \hat{\mathbf{x}}}{\partial \overline{\mathbf{y}}}\right]^T \Sigma_\mathbf{y}\left[\frac{\partial \hat{\mathbf{x}}}{\partial \overline{\mathbf{y}}}\right] = [\mathbf{F}+\mathbf{R}]^{-1}\mathbf{F}[\mathbf{F}+\mathbf{R}]^{-1} \tag{15}$$

Spectral CT data with less noise, greater resolution, or greater separability will improve the precision, or the amount of information in **F**, which will lower the variability in $\hat{\mathbf{x}}$. Higher regularization can decrease the noise but at the cost of a biased solution as described by (14).

From estimation theory, we known the Cramer-Rao lower bound on the covariance of unbiased estimators is $\boldsymbol{\Sigma}_\mathbf{x} \geq \mathbf{F}^{-1}$. From (14) and (15), we can see that as the regularization approaches zero, the transfer function approaches identity and the covariance approaches the inverse of the Fisher information matrix. Assuming that **F** is invertible, this satisfies the condition for an efficient unbiased estimator, achieving equality to the Cramer-Rao lower bound. In practice, SSF CT systems typically result in a non-invertible or poorly conditioned **F** so some spatial regularization is necessary.

3) Detectability: We aim to apply these expressions for the signal transfer function and covariance to a single quality metric for the detectability of a signal, **w**. For relatively small signals, where the linearity approximation holds, we can express the detectability index as

$$d^2(\mathbf{w}) = \mathbf{w}^T\left[\frac{\partial\hat{\mathbf{x}}}{\partial\mathbf{x}}\right]^T\boldsymbol{\Sigma}_{\mathbf{x}}^{-1}\left[\frac{\partial\hat{\mathbf{x}}}{\partial\mathbf{x}}\right]\mathbf{w} = \mathbf{w}^T\mathbf{F}\mathbf{w} \tag{16}$$

This formulation of detectability index represents the performance of an ideal observer with exact knowledge of the background, the signal, and the noise covariance and is tasked with determining the presence or absence of the known signal, **w**, in the presence of noise.

It is important to note that for spectral CT, detectability index does not tell the full story. For example, in water/iodine imaging, a CT system may have high detectability for a known iodine contrast signal. Even a single-energy CT system would be capabe of detecting the presence or absence of this signal but that does not mean it would be effective at telling whether that signal came from iodine or soft tissue. Thus, there is a need for a quantitative definition of material separability which distinguishes spectral CT systems from single-energy systems.

4) Separability: Spectral CT systems are capable of enhanced material discrimination in comparison to conventional CT. To illustrate the importance of material separability, Figure 3 shows an example of (iodine/water) material density estimates which can be achieved with a dual-energy CT system. Note that the noise is highly anti-correlated between materials which is a consequence of poor material separability. The first three columns represent the following stimuli, respectively: 1) a positive water density impulse, 2) a positive iodine impulse, and 3) an impulse of both iodine and water. We note that even a single-energy CT system will yield a relatively high detectability index for these tasks since there is no need to determine whether the measured signal is coming from an increased density of water versus iodine. The fourth column shows a stimulus that is a water impulse minus an iodine impulse (e.g. decreased iodine uptake with respect to some baseline). For a single-energy CT system, detection of this stimulus can be difficult to differentiate with the absence of any signal at all; whereas spectral CT should have a distinct advantage. There is need for a quantitative metric which summarizes this separability which distinguishes spectral CT systems. While performance generally increases with increased x-ray exposures, we would like to decouple overall exposure from system design. Therefore, we propose the following normalized formulation for the separability index:

$$s^2_{k_1,k_2} = \frac{\left(\mathbf{w}_{k_1} - \mathbf{w}_{k_2}\right)^T\mathbf{F}\left(\mathbf{w}_{k_1} - \mathbf{w}_{k_2}\right)}{\left(\mathbf{w}_{k_1} + \mathbf{w}_{k_2}\right)^T\mathbf{F}\left(\mathbf{w}_{k_1} + \mathbf{w}_{k_2}\right)} \tag{17}$$

where $\mathbf{w}_{k_1}$ and $\mathbf{w}_{k_2}$ are identical spatial signals corresponding to different materials. Moreover, we scale the stimuli such that $d^2\left(\mathbf{w}_{k_1}\right) = d^2\left(\mathbf{w}_{k_2}\right)$. This metric can be interpreted as a ratio of the detectability of the material-differentiating task and the material-integrating task.

$$s^2_{k_1,k_2} = \frac{d^2(\mathbf{w}_{k_1} - \mathbf{w}_{k_2})}{d^2(\mathbf{w}_{k_1} + \mathbf{w}_{k_2})} \tag{18}$$

The definition given in (17) and (18) applies to a two-material imaging case but there is a need for a generalized definition which can apply to the case of imaging three or more materials. For this generalization of separability, we define a new cross material matrix **C** which is constructed from **F** and the single-material task functions $\mathbf{w_{k_n}}$ (with the same spatial distribution) as shown below

$$C_{k_n,k_m} = \frac{\mathbf{w}_{k_n}^T \mathbf{F} \mathbf{w}_{k_m}}{\sqrt{\mathbf{w}_{k_n}^T \mathbf{F} \mathbf{w}_{k_n}} \sqrt{\mathbf{w}_{k_m}^T \mathbf{F} \mathbf{w}_{k_m}}} \tag{19}$$

The ratio in (19) is a normalization which mirrors (17). As a result, the diagonal elements of **C** will be 1 and the off-diagonal elements will be between 0 and 1. Thus, the two-material separability may be written as

$$s^2 = \frac{[1, -1]\mathbf{C}[1, -1]^T}{[1, 1]\mathbf{C}[1, 1]^T} \tag{20}$$

Because on the form of **C**, (20) is equivalent to the ratio of the smaller to the larger eigenvalues of the 2 × 2 matrix. For three or more materials, we extend the definition of separability as the inverse of the condition number of **C**.

$$s^2 = \frac{1}{\text{cond}(\mathbf{C})} \tag{21}$$

This definition is compatible with three or more materials for cases such as water/calcium/gadolinium decomposition, or multi-contrast-enhanced imaging.

This definition allows quantification of separability and has several desirable properties. Given the following assumptions:

1. $\mathbf{w_{k_n}} \mathbf{F} \mathbf{w_{k_m}} > = 0$
2. $\mathbf{w_{k_n}} \mathbf{F} \mathbf{w_{k_n}} = \mathbf{w_{k_m}} \mathbf{F} \mathbf{w_{k_m}}$

the separability index can be shown to have the following properties:

1. Separability is bounded by [0, 1]
2. Separability is unitless
3. Separability is invariant for scalar multiplication of **F**
4. Separability is invariant for proportional scaling of the task functions, $\mathbf{w_{k_1}}, \ldots, \mathbf{w_{k_N}}$

5. Separability of a set of materials is less than or equal to the separability of any subset of those materials

Single-energy CT systems will generally have $s \approx 0$. There will typically be some small amount of information contained in the data due to beam hardening effects which change the sensitivity spectra, but it is generally considered insufficient for material decomposition. The case $s = 1$ would mean the material density information is immediately available from the measurements. This is not possible with standard tomographic system designs, in part, due to the large overlap between mass attenuation spectra of physical materials.

The separability index is a quantitative metric for how well conditioned the material decomposition portion of the problem will be. Independence to the scale of **F** means that separability does not change based on the x-ray source power or exposure time. Separability depends on noise correlations, not noise magnitude. It is a task-specific method to describe the conditioning of the material decomposition problem using nonlinear physical models. It can be used to determine the feasibility of material decomposition for a specific spectral CT system and a specific set of two or more materials. We will show that it can also be used to optimize spectral CT system design for material discrimination tasks.

D. Design Optimization

In this section we present an experimental procedure to apply detectability and separability prediction to optimize the design of SSFs. In particular, we will simuluate a water/calcium/gadolinium imaging scenario for contrast-enhanced liver imaging. For this type of imaging, the water density shows soft tissue, calcium is useful for quantifying bone density as well as detected calcified lesions, and gadolinium density estimates show the concentration of an exogenous contrast agent. As we will show, it can also be useful to view monoenergetic attenuation images generated by weighted summation of material densities times mass attenuation coefficients at a certain photon energy level. Based on our understanding of detectability and separability, we hypothesize that a detectability-optimized design will be better at detecting the presence or absence of a small concentration of a known material, whereas a separability-optimized design will perform better at material discrimination.

To simulate SSF CT, we use the physical models presented in previous sections to model a cone-beam CT (CBCT) system with a 1100 mm source-to-detector distance, 830 mm source-to-axis distance, 0.556 mm pixel spacing, 360 views per rotation, and 60 rotations per minute. These geometric parameters are designed to match a configuration that can be achieved on a realistic CBCT system. The focal spot size was assumed to be 0.5 mm and our physical model includes focal spot blur including spectral mixing effects. The simulated SSF was positioned 380 mm from the source. The image space used for reconstruction is two-dimensional with 512 × 512 × 11mm cubic voxels. We used 6 to normalize the exposure settings such that 5mJ was attenuated in the water tank for fair comparisons between different designs.

The filter tile motion trajectory is generated by a velocity square-wave with a constant speed of 120 mm/s for 1 second (or 60 views) followed by the same speed in the opposite direction for another 6 seconds and then repeating. Note that the same sampling pattern would be

possible with faster rotation speeds if the translation speed is scaled accordingly. We fix the length of one period of filter tiles to 60 mm so that each 6 second interval covers two periods of the filter. Since the filter motion is linear, the proportion of the filter length taken up by a material is roughly the same as the proportion of views which are filtered by that material for a certain fan angle. For example, if 20% of the SSF is gold, then roughly 20% of the views will be gold-filtered for a given detector.

The free parameters for the SSF design optimization experiment are the filter tile materials, filter tile width, filter tile thickness and source voltage. These parameters are used to generate the voxelized multi-material SSF model with 100 μm × 10 μm voxel size (smaller dimension is for filter thickness). Since the entire simulation is two-dimensional, the SSF model is also two-dimensional (1 mm thickness). We assume every design will use three filter tile types. We limit our filter tile materials and thicknesses to the list shown in Figure 4 which are affordable and accessible. To enforce realistic designs, we excluded any filter options which resulted in < 10% transmission for a polyenergetic x-ray source at 100 kVp. This constraint resulted in the exclusion of any 500 μm filters as well as 250 μm filters made of Lu, Ta, Au, and Pb. We limited the minimum filter tile width to 5 mm and the total filter period is fixed at 60 mm. K-edge filters will always require more x-ray source power. By limiting filter transmission to 10%, the worst case scenario for a CT system with SSF upgrade would be scan times which are ten times as long. However, most systems are capable of higher source current that would mitigate this potential time penalty.

We used simulations to find optimized designs for two tasks: water/calcium/gadolinium separability and gadolinium detectability. For a realistic model of the challenges of a non-linear imaging scenario, we evaluated these tasks for a 1mm voxel at the center of a 320 mm diameter digital water tank phantom as shown in Figure 5. Using this phantom, our goal is to design SSFs for high performance in water/calcium/gadolinium imaging in human patients.

The numerical optimization of the SSF design was conducted using a brute force categorical search over all combinations of 3 of the 12 valid filter materials and thicknesses from the list in Figure 4. For each case, filter widths and peak source voltage were optimized iteratively using 1000 iterations of the CMAES solver [24]. In this way, we identified the design with the highest three-material separability of water/calcium/gadolinium as well as the design with the highest detectability of small concentrations of gadolinium.

Simple phantoms such as this water tank are used as a standardized object for many applications such as calibration or design optimization. However, it is important to verify that these designs are suitable for a human patient. The next section describes how these designs were applied and evaluated via a more clinically realistic water/calcium/gadolinium scenario.

E. Performance Evaluation with Anthropomorphic Phantoms

After the optimized designs for gadolinium detectability and water/calcium/gadolinium separability have been identified, our next step is to evaluate their performance for clinically meaningful tasks. In particular, our goal is to test our hypothesis that optimizing for detectability is ideal for determining the presence of absence of small concentrations of

a known material, whereas optimizing for separability is ideal for determining the material composition of an object.

To this end, we used the XCAT digital anthropomorphic phantom generator [25] to create ground-truth material density images which are intended to resemble a clinically realistic scenario. We used the XCAT interface to generate 3D patient attenuation images with 1mm voxels from which we extracted 1000 2D axial slices. We generated 50 male and 50 female phantoms using randomized anatomical parameters with the mean set to the XCAT defaults and with 10% FWHM (uncorrelated multivariate normal samples). For further variety of patient size/shape, we applied a ±10% scale independently for the long and short patient axes for each extracted 2D axial slice.

We generated images for 100 keV attenuation and 150 keV attenuation and used an idealized image-domain material decomposition with a non-negativity constraint to produce water density and calcium density ground truth images. We used the activity image feature (originally intended to create PET activity biodistributions) to create gadolinium density images with 10 ± 2 mg/mL Gd in the liver and 20 ± 4 mg/mL Gd in the veins which is our rough model of portal venous phase contrast enhancement for liver images. Figure 6 shows an example of a multi-material digital anthropomorphic phantom. While this phantom differs from a realistic human patient in many ways, it is designed to be an approximation for the purpose of evaluating the SSF designs in simulation.

We used our physical models to generate noisy SSF projection data for the optimized designs using the phantom shown in Figure 6. We ran 1000 iterations of the MBMD reconstruction described in a previous section including a quadratic smoothness penalty with cross-material weights described in [20]. The magnitude of this penalty term was set to ≈ 1% of the data fidelity term to keep bias/blur at a relatively low level. This was accomplished by computing a block-diagonal approximation of the Fisher information matrix following the methods in [26] and setting the penalty weights (including cross-material penalty weights) to 1% of those values. An example of the simulated noisy SSF CT measurements is shown in Figure 7.

This simulation of SSF CT measurements and reconstruction of noisy multi-material density images was repeated several lesion-shaped perturbations in the liver (shown in Figures 11 and 12) for the anatomical background shown in Figure 6. First, we simulated a scenario where the lesion consisted of 3 HU (at 70 keV) of gadolinium. Second, we simulated a scenario where the lesion consisted of −60 HU of water, +30 HU of calcium and +30 HU of gadolinium. The first task is designed to showcase the gadolinium detectability of each design, whereas the second task is designed to showcase the water/calcium/gadolinium separability of each design.

Finally, to evaluate the effect of patient size on performance, we computed detectability and separability metrics each of the 1000 2D phantoms for a voxel at the center of the patient. We computed the detectability index of +10 HU (at 70 keV) of water and +10 HU of gadolinium (the integral detectability), the detectability index of +10 HU of water and

−10 HU of gadolinium (the differential detectability), and the water/gadolinium separability index.

III. Results

From the SSF optimization experiment, we identified two optimized system designs. As shown in Figure 8, the optimized SSF CT design for water/calcium/gadolinium separability in the 320 mm water tank is composed of 14.17 mm × 250 μm Sn, 40.83 mm × 250 μm Gd, and 5.00 mm × 100 μm Au filter tiles with a peak source voltage of 127.4 kV. If the number of photons interacting with the central detector are integrated for all views, 29.9% of photons are filtered by Sn, 61.6% are filtered by Gd, and 8.5% are filtered by Au. These are relatively thick filters which result in more distinct transmission spectra as shown in Figure 9. The Au filter tile has the minimum width of 5.00 mm whereas the 40.83 mm × 250 μm Gd filter tile is very large and will be applied to over half of the measurements in the projection domain. The K-edge of gadolinium at 50.2 keV is likely very useful for distinguishing exogenous gadolinium contrast agents from endogenous water/calcium in the patient. The relatively high source voltage of 127.4 kV will result in a broad spectrum of incident photon energies which may be very useful when distinguishing three different materials.

As shown in Figure 8, the optimized SSF CT design for gadolinium detectability in the 320mm water tank is composed of 5.00 mm × 250 μm Sn, 35.50 mm × 100 μm Au, and 19.50 mm × 100 μm Pb filter tiles with a peak source voltage of 94.3 kV. If the number of photons interacting with the central detector are integrated for all views, 8.7% of photons are filtered by Sn, 48.4% are filtered by Au, and 42.9% are filtered by Pb. This design has a lower source voltage and thinner filters which indicate that it is focused on the lower energy range. This does make sense for this gadolinium detectability task since gadolinium attenuation is very strong in the range of 50–60 keV due to its K-edge at 50.2 keV. The 100 μm Pb filter and 100 μm Au filter seem to be excellent selections for selective transmission in this energy range as shown in Figure 9.

Figure 10 shows the MBMD results for the separability-optimized design applied to the phantom shown in Figure 6. Despite the fact that SSF CT measurements are sparse in the projection domain for each filter, it is still possible to reconstruct multi-material images via regularized MBMD. There are streak artifacts visible in the gadolinium concentration and attenuation images which we believe is due to non-uniform spatial-spectral sampling. Previous studies have revealed that faster filter motion speeds can improve the uniformity of spatial-spectral sampling [12] In this work we consider only one static linear filter motion profile. A more comprehensive design optimization including SSF trajectories will be investigated in future work for potential mitigation of these artifacts. There are also visible cross-material errors, particularly in the liver, where overall attenuation is highest. This may be due to regularization which is known to produce some cross-material bias. It is also possible the errors would be reduced with more iterations of the MBMD algorithm. We also observe that the noise is strongly anti-correlated between materials. The noise variance appears higher in the individual material images than in the virtual monoenergetic image which is a weighted combination of all three materials. Finally, there are visible

spatial correlations which change for different parts of the image and different materials. This is likely due to the complex spatial-spectral sampling pattern of SSF CT. Combined with the effects of multi-material spatial regularization, this can produce spatially varying multi-material noise properties.

The perturbation reconstructions in a uniform region of the liver are shown in Figures 11 and 12. These help to highlight the difference in multi-material image quality for the two optimized designs. Figure 11 shows a lesion-shaped perturbation consisting of −60 HU (at 70 keV) of water, +30 HU of calcium, and +30 HU of calcium. For a single-energy CT system, this task would be nearly impossible since the net attenuation is zero. Spectral CT systems are distinguished from single-energy CT systems by their ability to determine the material composition of the signal. From 11 it appears that the separability-optimized design (design A) has superior performance for this task. Figure 12 shows a +3 HU gadolinium perturbation. In this case, the virtual monoenergetic attenuation image is not zero since the net attenuation is +3 HU. It appears that signal to noise ratio in the attenuation image is best for the detectability-optimized design (design B). These results confirm our hypothesis that the separability-optimized design is superior for material discrimination, and the detectability-optimized design is superior for detection of small concentrations of known materials. Figure 13 shows detectability and separability as a function of patient size for the two optimized designs. The first plot is integral detectability, meaning the detectability index of +10 HU of water and +10 HU of gadolinium at the center of the patient. The second plot is differential detectability, meaning the detectability of +10 HU of water and −10 HU of gadolinium for a voxel at the center of the patient. The third plot is water/gadolinium separability index. Note that the third plot is similar to the ratio of the second plot to the third plot but not exactly the same. For the first two plots, the same density of water and gadolinium were used for all patients regardless of the nonlinear weights for that particular patient's attenuation spectra. To compute separability for the third plot, those two tasks are effectively normalized by their detectability for each patient before taking the ratio as previously described.

The first plot in Figure 13 shows that the detectability-optimized design is superior for detecting the positive water positive gadolinium signal for all patient sizes. The second plot shows that the separability-optimized design is superior for detecting the positive water negative gadolinium signal for all patient sizes. Both detectability metrics are decreased for larger patient sizes; however, the third plot shows that separability index is approximately constant for different patient sizes. Water/gadolinium separability is significantly higher for the separability-optimized design than for the detectability-optimized design as expected.

IV. Discussion and Conclusion

Spectral CT with spatial-spectral filters is a promising new technology which enables enhanced material discrimination, quantitative material density estimation, and multi-material decomposition. SSFs offer a method for adding spectral capability to existing CT systems without modifications to the source and with ordinary energy-integrating detectors. In this work we have presented a generalized physical model for spectral CT and showed how it can be applied to model spatial-spectral filters and conduct a model-

based material decomposition. We introduced a new image quality metric for spectral CT based on detectability to quantify separability. Finally, we presented a design optimization experiment, where the design parameters were tuned to maximize separability index for small and large patients, as well as two different material separation cases.

One limitation of the physical model used in this work was the neglect of scatter. The SSF is positioned near the source, so we expect that any scattering which occurs in the filter tiles will result in low-spatial-frequency changes to the signal due to the effects of magnification. Scattering inside the object/patient could also have an impact. Furthermore, scattering is a photon-energy dependent phenomenon, so this could have complex effects on material density estimation. Patient motion is another potential source of error that should be addressed for practical application of this device. In the future, we aim to explore these more advanced effects using higher-fidelity physical models for MBMD. Another limitation is that the performance optimization tools for detectability and separability are based on the Fisher information matrix for the system. That is, they describe the properties of unbiased estimators with no dependence on regularization. While we expect regularization to be an important part of producing good clinical images, we have decoupled the system design and regularization aspects in this work. A more sophisticated system optimization approach would be to jointly estimate system design and regularization.

Regarding our proposed separability index, we note that one pre-existing alternative is the dual-energy index [27] which is defined based on contrast in the image domain as follows:

$$\mathrm{DEI} = \frac{\mathrm{HU}_1 - \mathrm{HU}_2}{\mathrm{HU}_1 + \mathrm{HU}_2} \tag{22}$$

where HU_1 and HU_2 are the Hounsfield units at two different photon energy levels. This has some similarities with the proposed separability index since there is a differential contrast in the numerator normalized by an integral contrast in the denominator. Furthermore, this dual-energy index is a property of materials, not imaging systems. We believe our metric has several advantages because it takes into account a nonlinear physical model and the effects of multi-material noise correlations. Another benefit to the separability index is that it can be used to quantify the capability of an imaging system to separate three or more specific materials as we have demonstrated in this work.

Regarding the simulated clinical application, we acknowledge gadolinium is not commonly used as a CT contrast agent. However, gadolinium-based contrast agents are clinically approved and commonly used for MRI contrast enhancement and are being investigated for spectral CT applications. [3] [28]. As described in Appendix I, the separability index of water/calcium/gadolinium decomposition is approximately ten times higher than water/calcium/iodine decomposition. The amount of gadolinium we simulated is in the same range as the concentrations measured in the liver in [3]. This analysis provides support for the use of gadolinium-based contrast agents for clinical applications of spectral CT and material decomposition in the presence of calcium such as bones or calcified lesions.

Another limitation we acknowledge is that all designs were optimized based on separability at the center of a water tank and so, for example, they will not necessarily be optimal designs for objects at the edge of the water tank. From, Figure 13, we can see that variation in anatomical background can lead to significant variation in separability index for the same system design.

One unexpected result was the relatively high variability of detectability and separability indices for different patients with the same water-equivalent diameter as shown by the error bars in Figure 13. The scatter plot seems to show bimodal streaks which have not yet been identified. This may be related to the impact different patient anatomical shapes with the same water-equivalent diameter (e.g. different axial levels). We hope to conduct an investigation into the effects patient size and shape in the future.

Spatial-spectral filters have a flexible design framework which can be tuned based on the task of interest and the imaging target. While we have demonstrated the importance of design and illustrated success of such filters in simulation, there are likely engineering challenges for practical implementation in a clinical CT gantry. Prior studies with other dynamic filters [29] [30] suggest that such moving filters are possible. While we have demonstrated good performance across a range of patient sizes, different tasks do significantly influence the SSF design. As such, future work should consider how to integrate multiple SSF designs within one system (e.g. via swappable filters, different filter motions, two-dimensional filters, etc.). Additionally, the spatial-spectral filtering concept can be combined with other spectral techniques for improved separability [31]. In the future, we are interested in using SSFs and kV-switching, or SSFs and energy-discriminating detectors in hybrid spectral CT systems to improve imaging performance, separability, and quantitation of small changes to concentration or density.

Acknowledgments

This work was supported, in part, by NIH grant R21EB026849.

This work was supported, in part, by NIH grant R01EB030494.

Appendix I

Separability Index of Different Basis Materials

One potential application of the newly proposed separability index is to quantitatively evaluate the feasibility of combinations of basis materials for given specific background conditions and spectral CT system designs. In particular, for this work we evaluate the feasibility of water/calcium/iodine decomposition or water/calcium/gadolinium decomposition

We analyzed combinations of the basis materials shown in Figure 14. For background conditions, we consider the center of a 320mm diameter water cylinder, and for system design, we consider a kVp control spectral CT system with source spectra as shown in Figure 15, and total system sensitivity spectra shown in Figure 16. After attenuation from 320mm of water, beam hardening results in the sensitivity spectra shown in Figure 17.

Under these conditions, the separability index of water/calcium/iodine is 0.272% which, for comparison, makes it less feasible than water/fat separability which is 1.068%. The separability index of water/calcium/gadolinium is approximately ten times higher at 2.685%.

References

[1]. Bhayana R, Parakh A, and Kambadakone A, "Material decomposition with dual-and multi-energy computed tomography," MRS Communications, vol. 10, no. 4, pp. 558–565, 2020.

[2]. Suzuki K, "A review of computer-aided diagnosis in thoracic and colonic imaging," Quantitative imaging in medicine and surgery, vol. 2, no. 3, p. 163, 2012. [PubMed: 23256078]

[3]. Muenzel D, Daerr H, Proksa R, Fingerle AA, Kopp FK, Douek P, Herzen J, Pfeiffer F, Rummeny EJ, and Noël PB, "Simultaneous dual-contrast multi-phase liver imaging using spectral photon-counting computed tomography: a proof-of-concept study," European radiology experimental, vol. 1, no. 1, p. 25, 2017. [PubMed: 29708205]

[4]. Rassouli N, Etesami M, Dhanantwari A, and Rajiah P, "Detector-based spectral ct with a novel dual-layer technology: principles and applications," Insights into imaging, vol. 8, no. 6, pp. 589–598, 2017. [PubMed: 28986761]

[5]. Leng S, Bruesewitz M, Tao S, Rajendran K, Halaweish AF, Campeau NG, Fletcher JG, and McCollough CH, "Photon-counting detector ct: system design and clinical applications of an emerging technology," Radiographics, vol. 39, no. 3, pp. 729–743, 2019. [PubMed: 31059394]

[6]. Flohr TG, McCollough CH, Bruder H, Petersilka M, Gruber K, Süβ C, Grasruck M, Stierstorfer K, Krauss B, Raupach R et al. , "First performance evaluation of a dual-source ct (dsct) system," European radiology, vol. 16, no. 2, pp. 256–268, 2006. [PubMed: 16341833]

[7]. Zou Y and Silver MD, "Analysis of fast kv-switching in dual energy ct using a pre-reconstruction decomposition technique," in Medical Imaging 2008: Physics of Medical Imaging, vol. 6913. SPIE, 2008, p. 691313.

[8]. Rutt B and Fenster A, "Split-filter computed tomography: a simple technique for dual energy scanning." Journal of computer assisted tomography, vol. 4, no. 4, pp. 501–509, 1980. [PubMed: 7391293]

[9]. Euler A, Parakh A, Falkowski AL, Manneck S, Dashti D, Krauss B, Szucs-Farkas Z, and Schindera ST, "Initial results of a single-source dual-energy computed tomography technique using a split-filter: assessment of image quality, radiation dose, and accuracy of dual-energy applications in an in vitro and in vivo study," Investigative radiology, vol. 51, no. 8, pp. 491–498, 2016. [PubMed: 26895193]

[10]. Petrongolo M and Zhu L, "Single-scan dual-energy ct using primary modulation," IEEE transactions on medical imaging, vol. 37, no. 8, pp. 1799–1808, 2018. [PubMed: 29994601]

[11]. Tivnan M, Tilley II S, and Stayman JW, "Physical modeling and performance of spatial-spectral filters for ct material decomposition," in Medical Imaging 2019: Physics of Medical Imaging, vol. 10948. SPIE, 2019, p. 109481A.

[12]. Tivnan M, Wang W, Tilley II S, Siewerdsen JH, and Stayman JW, "Optimized spatial-spectral ct for multi-material decomposition," in Fully 3D, vol. 11072. International Society for Optics and Photonics, 2019, p. 1107211.

[13]. Tivnan M, Wang W, Tilley S, and Stayman J, "Designing spatial-spectral filters for spectral ct," in MEDICAL PHYSICS, vol. 46. WILEY 111 RIVER ST, HOBOKEN 07030–5774, NJ USA, 2019, pp. E407–E407.

[14]. Tivnan M, Wang W, and Stayman JW, "Multi-contrast ct imaging with a prototype spatial-spectral filter," in Conference proceedings. International Conference on Image Formation in X-Ray Computed Tomography, vol. 2020. NIH Public Access, 2020, p. 638. [PubMed: 33163990]

[15]. Wang Z, Feng Y, and Jia Y, "Spatial-spectral compressive sensing of hyperspectral image," in 2013 IEEE Third International Conference on Information Science and Technology (ICIST). IEEE, 2013, pp. 1256–1259.

[16]. Tilley S and Stayman J, "Model-based material decomposition for acquisitions with relaxed spectral and spatial sampling," in Medical Physics, vol. 45, 2018, pp. E387–E387.

[17]. Barber RF, Sidky EY, Schmidt TG, and Pan X, “An algorithm for constrained one-step inversion of spectral ct data,” Physics in Medicine & Biology, vol. 61, no. 10, p. 3784, 2016. [PubMed: 27082489]

[18]. Siewerdsen J, Antonuk L, El-Mohri Y, Yorkston J, Huang W, Boudry J, and Cunningham I, “Empirical and theoretical investigation of the noise performance of indirect detection, active matrix flat-panel imagers (amfpis) for diagnostic radiology,” Medical physics, vol. 24, no. 1, pp. 71–89, 1997. [PubMed: 9029542]

[19]. Long Y and Fessler JA, “Multi-material decomposition using statistical image reconstruction for spectral ct,” IEEE transactions on medical imaging, vol. 33, no. 8, pp. 1614–1626, 2014. [PubMed: 24801550]

[20]. Wang W, Tivnan M, Gang GJ, and Stayman JW, “Prospective prediction and control of image properties in model-based material decomposition for spectral ct,” in Medical Imaging 2020: Physics of Medical Imaging, vol. 10948. SPIE, 2020, p. 109481A.

[21]. Tivnan M, Wang W, and Stayman JW, “A prototype spatial-spectral ct system for material decomposition with energy-integrating detector,” Medical physics, 2021.

[22]. Fessler JA and Rogers WL, “Spatial resolution properties of penalized-likelihood image reconstruction: space-invariant tomographs,” IEEE Transactions on Image processing, vol. 5, no. 9, pp. 1346–1358, 1996. [PubMed: 18285223]

[23]. Wang W, Tilley II S, Tivnan M, and Stayman JW, “Local response prediction in model-based ct material decomposition,” in Fully3D, vol. 11072. SPIE, 2019, p. 110720Z.

[24]. Hansen N, “The cma evolution strategy: a comparing review,” in Towards a new evolutionary computation. Springer, 2006, pp. 75–102.

[25]. Segars WP, Sturgeon G, Mendonca S, Grimes J, and Tsui BM, “4d xcat phantom for multimodality imaging research,” Medical physics, vol. 37, no. 9, pp. 4902–4915, 2010. [PubMed: 20964209]

[26]. Tivnan M, Wang W, and Stayman JW, “A preconditioned algorithm for model-based iterative ct reconstruction and material decomposition from spectral ct data,” arXiv preprint arXiv:2010.01371, 2020.

[27]. Leschka S, Fornaro J, Laberke P, Blum S, Hatem A, Niederer I, Meile C, Hibbeln D, Hausmann R, Wildermuth S et al. , “Differentiation of cocaine from heroine body packs by computed tomography: impact of different tube voltages and the dual-energy index,” Journal of forensic radiology and imaging, vol. 1, no. 2, pp. 46–50, 2013.

[28]. Nadjiri J, Pfeiffer D, Straeter AS, Noël PB, Fingerle A, Eckstein H-H, Laugwitz K-L, Rummeny EJ, Braren R, and Rasper M, “Spectral computed tomography angiography with a gadolinium-based contrast agent,” Journal of thoracic imaging, vol. 33, no. 4, pp. 246–253, 2018. [PubMed: 29863589]

[29]. Stayman JW, Mathews A, Zbijewski W, Gang G, Siewerdsen J, Kawamoto S, Blevis I, and Levinson R, “Fluence-field modulated x-ray ct using multiple aperture devices,” in Medical Imaging 2016: Physics of Medical Imaging, vol. 9783. International Society for Optics and Photonics, 2016, p. 97830X.

[30]. Liu F, Wang G, Cong W, Hsieh SS, and Pelc NJ, “Dynamic bowtie for fan-beam ct,” Journal of X-ray Science and Technology, vol. 21, no. 4, pp. 579–590, 2013. [PubMed: 24191994]

[31]. Tivnan M, Wang W, Gang GJ, Liapi E, Noël P, and Stayman JW, “Combining spectral ct acquisition methods for high-sensitivity material decomposition,” in Medical Imaging 2020: Physics of Medical Imaging, vol. 11312. International Society for Optics and Photonics, 2020, p. 1131218.

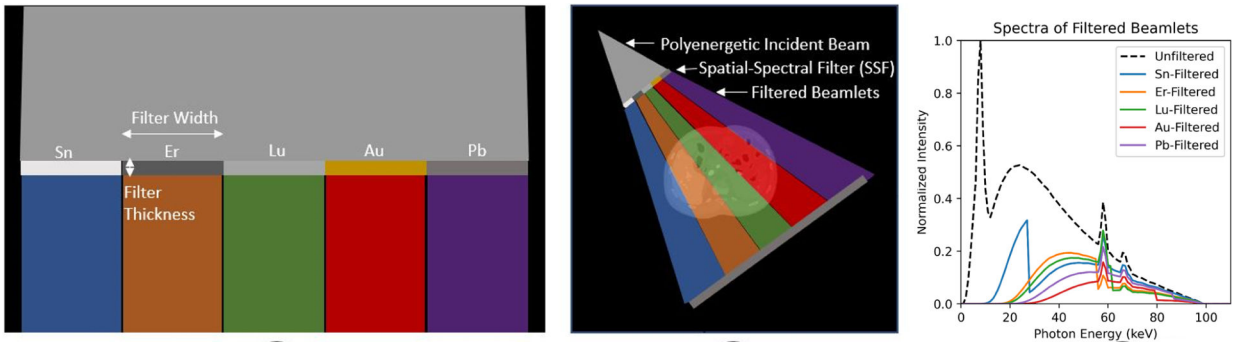

Fig. 1.

SSF example using Sn, Er, Lu, Au, and Pb filter materials. A polyenergetic beam generated by a 100kVp source is incident on the SSF which divides it into spectrally varied beamlets. The spectra on the right-hand plot make it clear there are discrete drops at the K-edge energy of each material.

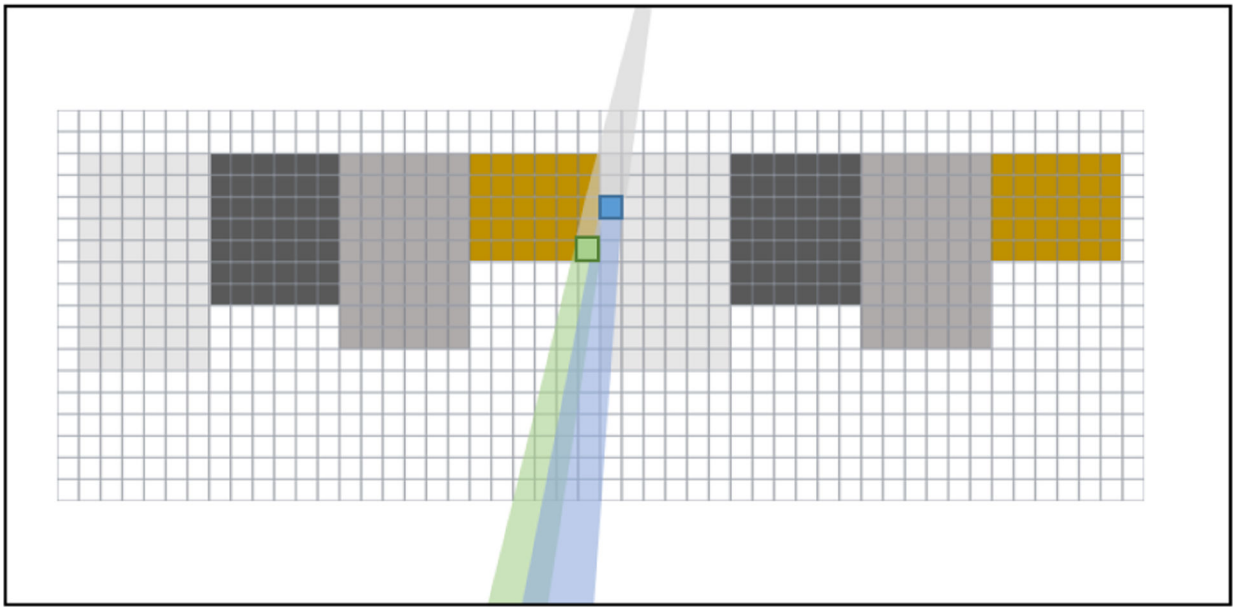

Fig. 2.
Forward projecting a high-resolution voxelized model for spatial-spectral filters enables models for varied geometric designs as well as spectral blur effects. Note that the diagram is not to scale.

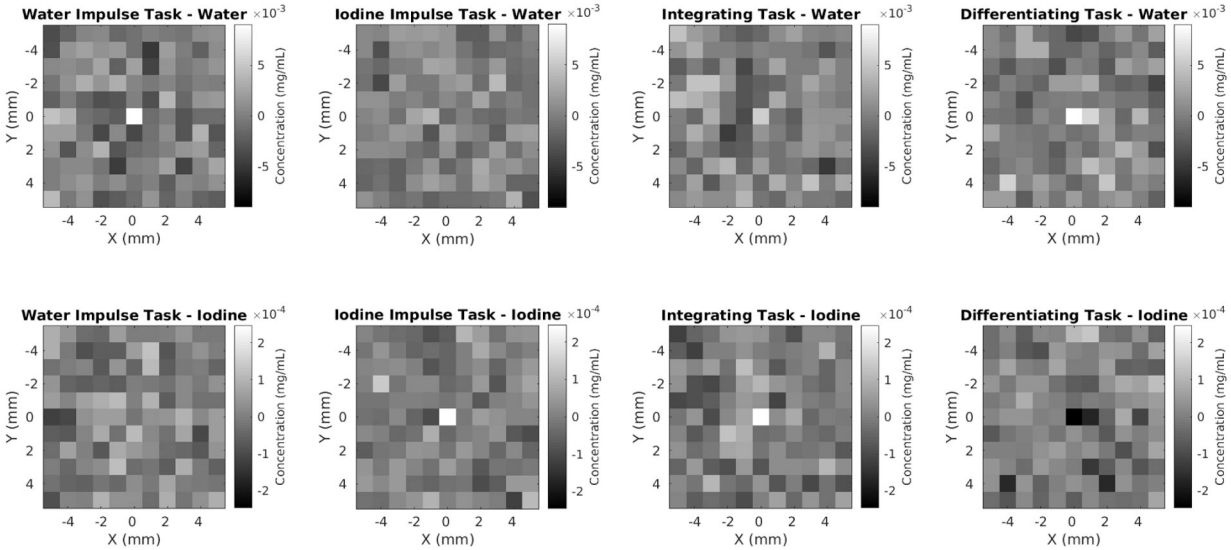

Fig. 3.

Reconstructed impulse stimuli in noise. Note that noise is anti-correlated between the water and iodine channels. Detectability index for the water task is 14.0, for the iodine task it is 14.0, for the integrating task (both impulses added) it is 27.7 and for the differentiating task (impulses subtracted) 4.8. Which results in a separability index of 0.174.

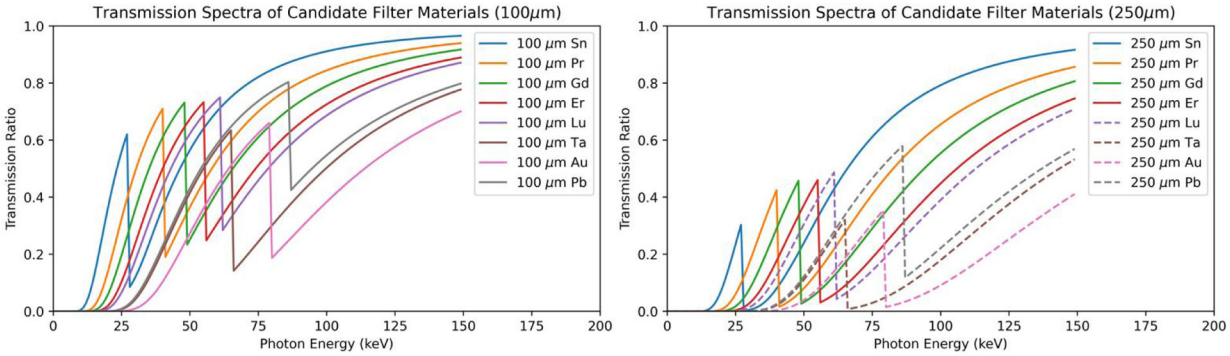

Fig. 4.

Ratio of transmitted to incident photons as a function of photon energy for candidate filter materials and thicknesses. The dotted lines show the designs which were excluded for having < **10**% effective transmission for a 100 kVp polyenergetic x-ray source.

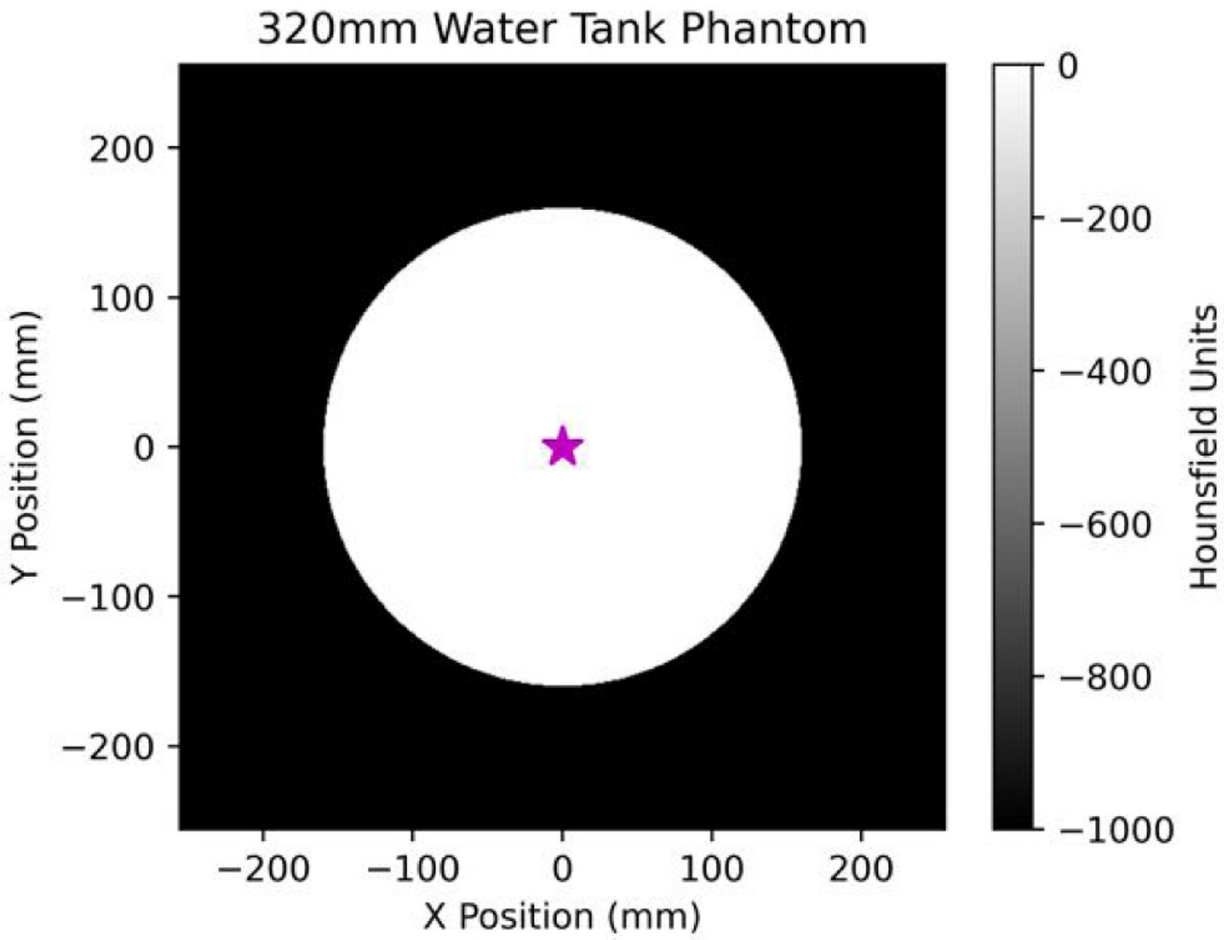

Fig. 5.
Digital phantom of a 320mm water tank. The star shows the voxel at which detectability and separability metrics are evaluated for the purposes of SSF design optimization.

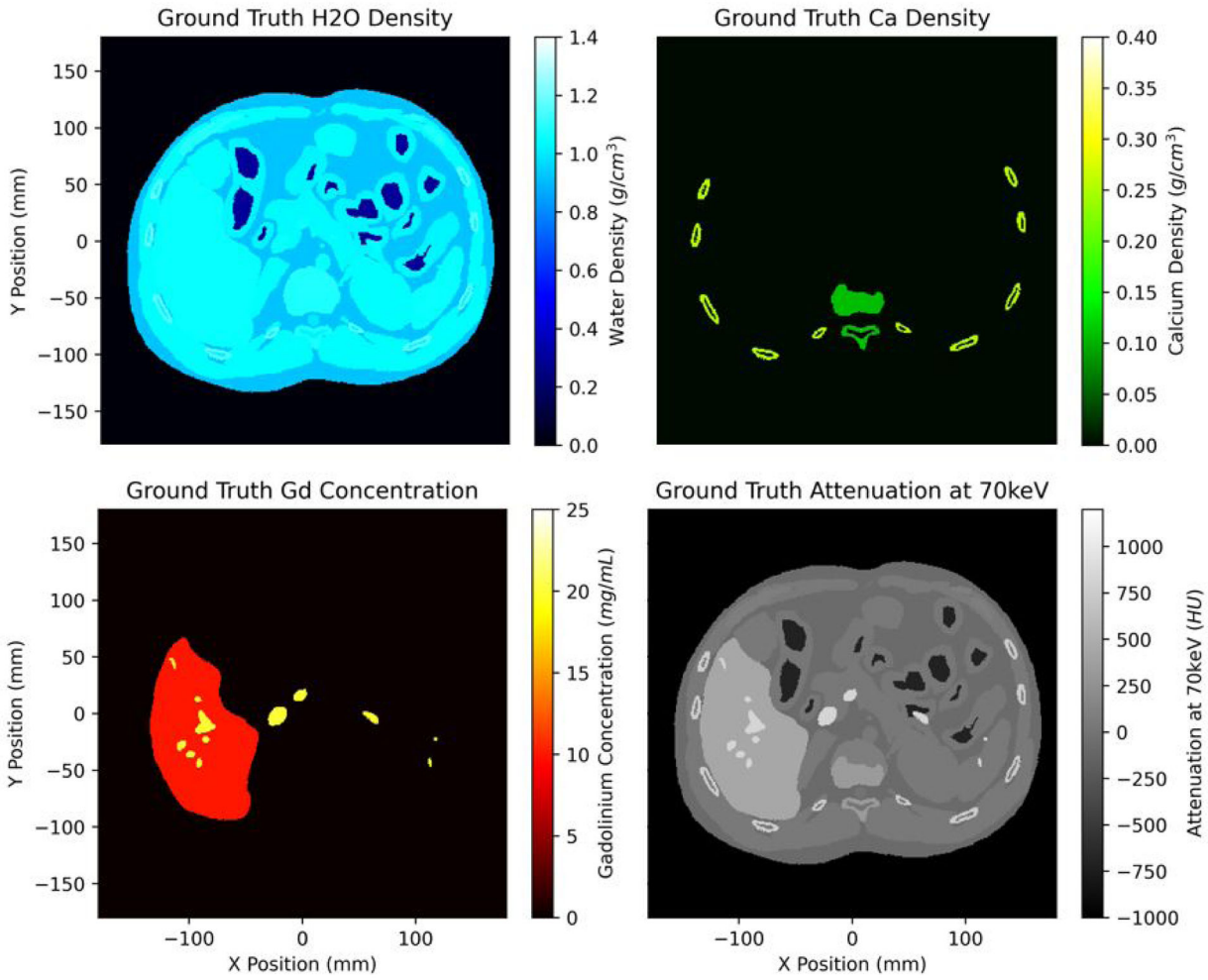

Fig. 6.

Multi-material anthropomorphic phantom based on XCAT designed to resemble a gadolinium-contrast-enhanced liver imaging scenario. The virtual monoenergetic attenuation image shown in the bottom right is a linear combination of the three material densities times mass attenuation coefficients at 70 keV.

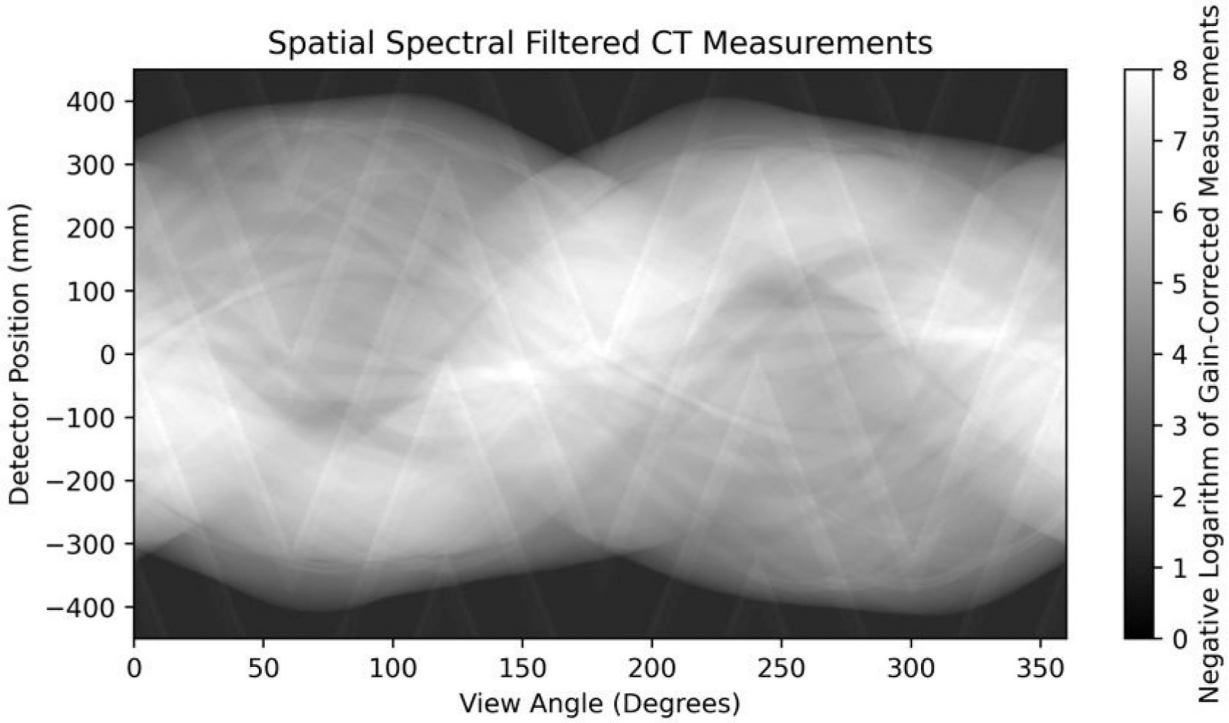

Fig. 7.

Simulated SSF CT measurements gain-corrected relative to the unfiltered case. The velocity square wave SSF trajectory results in a zig-zag pattern in the projection domain. Each filter spectra is sparse but with regularized model-based methods can be used for both reconstruction and material decomposition.

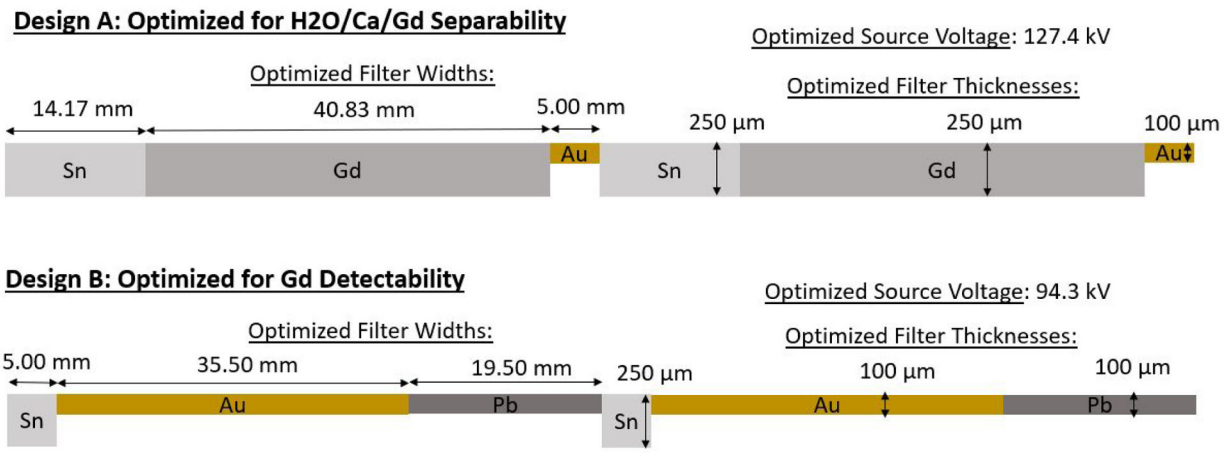

Fig. 8.

SSF Design A is optimized for water/calcium/gadolinium separability and consists of 14.17 mm × 250 μm Sn, 40.83 mm × 250 μm Gd, and 5.00 mm × 100 μm Au. Design B is optimized for Gd detectability and consists of 5.00 mm × 250 μm Sn, 35.50 mm × 100 μm Au, and 19.50 mm × 100 μm Pb.

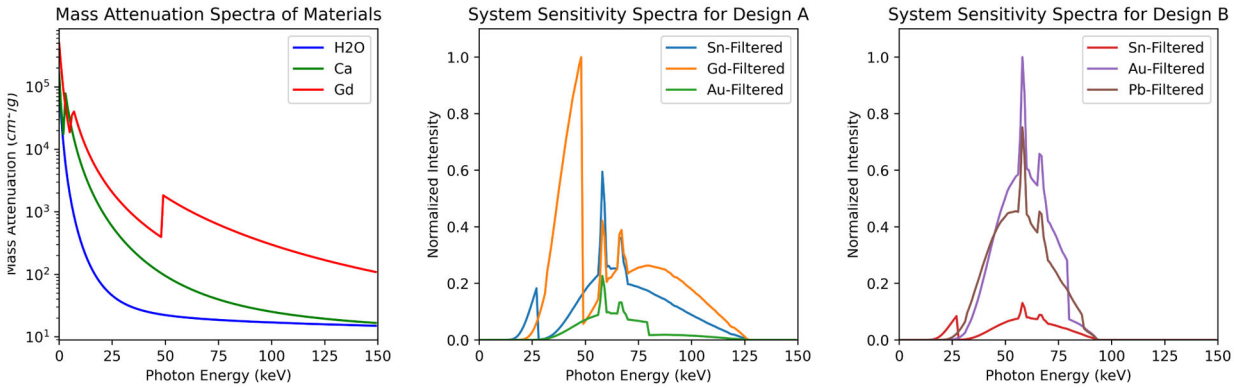

Fig. 9.

System sensitivity spectra for each design including source, filter, and detector spectra for the central detector integrated over all views.

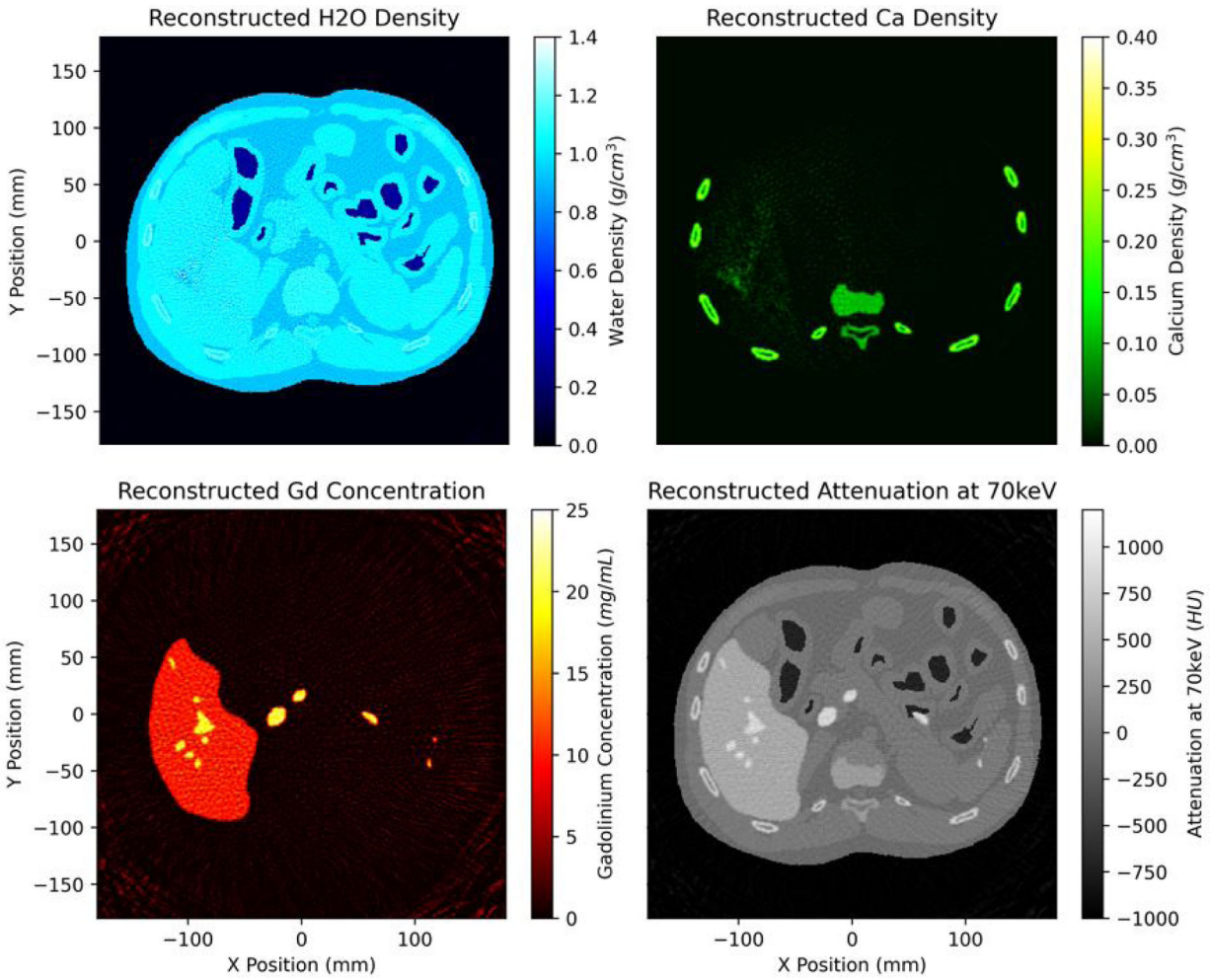

Fig. 10.

Water, calcium, and gadolinium density images and attenuation at 70 keV reconstructed using regularized model-based material decomposition from simulated SSF CT measurements.

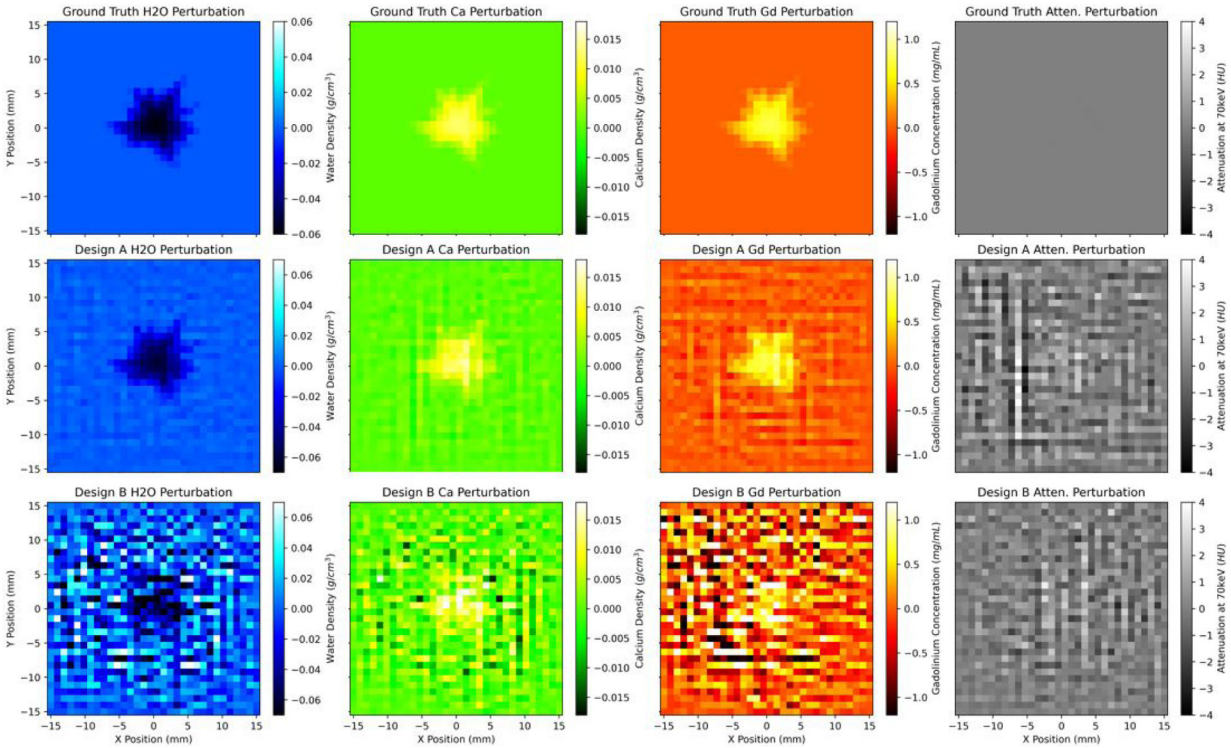

Fig. 11.

Reconstructed lesion perturbation in a uniform region of the liver containing −60 HU water, +30 HU calcium, +30 HU gadolinium. A single energy CT system would not be capable of detecting this signal as shown by the lack of contrast in the attenuation images. The material density images show that Design A, which is optimized for water/calcium/gadolinium separability, is the most capable at determining the material composition of this signal as expected.

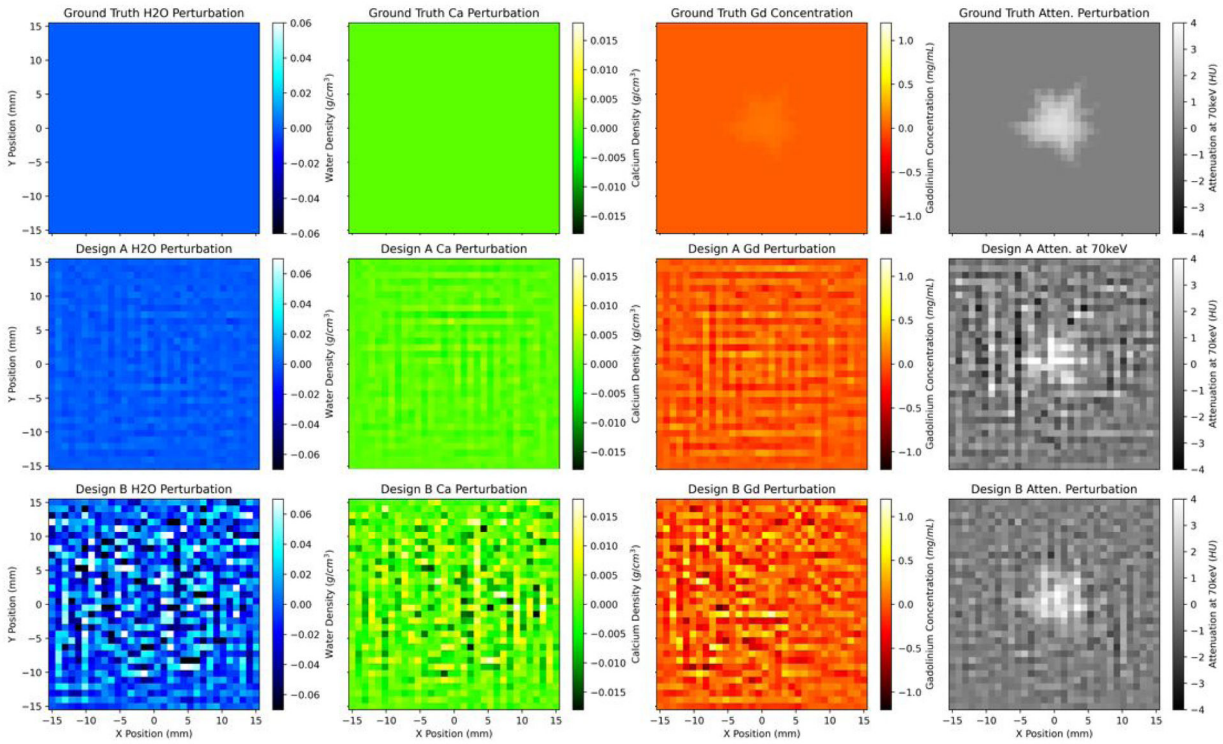

Fig. 12.

Reconstructed lesion perturbation in a uniform region of the liver containing +3 HU gadolinium. The signal is extremely hard to distinguish in the material density images. As expected, the virtual monoenergetic attenuation images show improved signal-to-noise ratio for Design B which was optimized for gadolinium detectability.

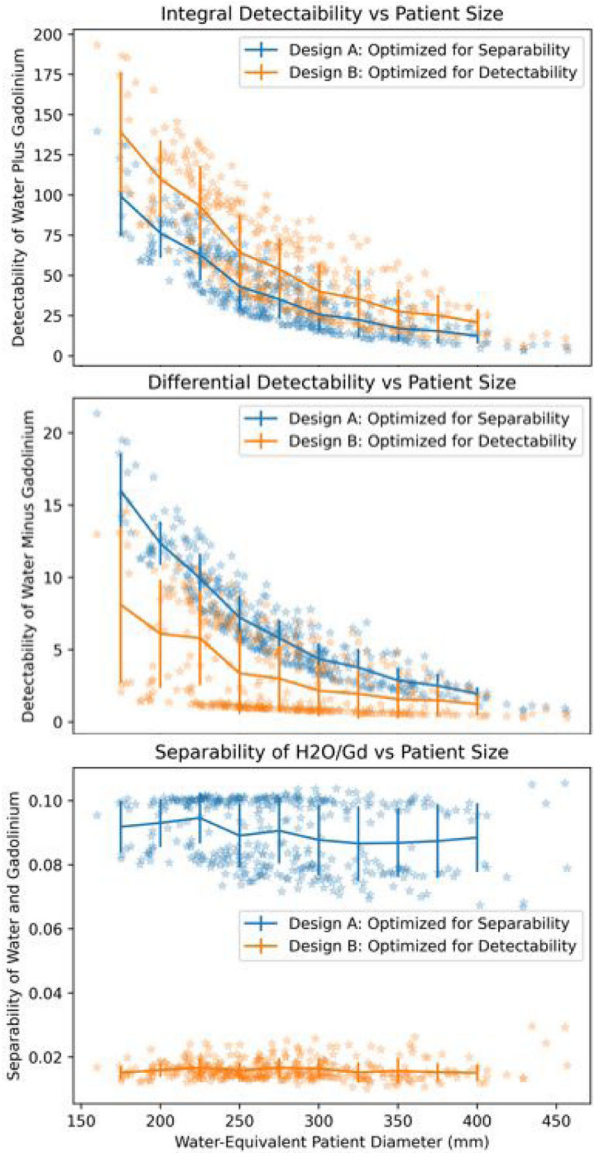

Fig. 13.

Integral detectability index, differential detectability index, and separability index of water and gadolinium. Scatterplot shows raw data and errorbars show population mean and standard deviation within discrete patient diameter bins.

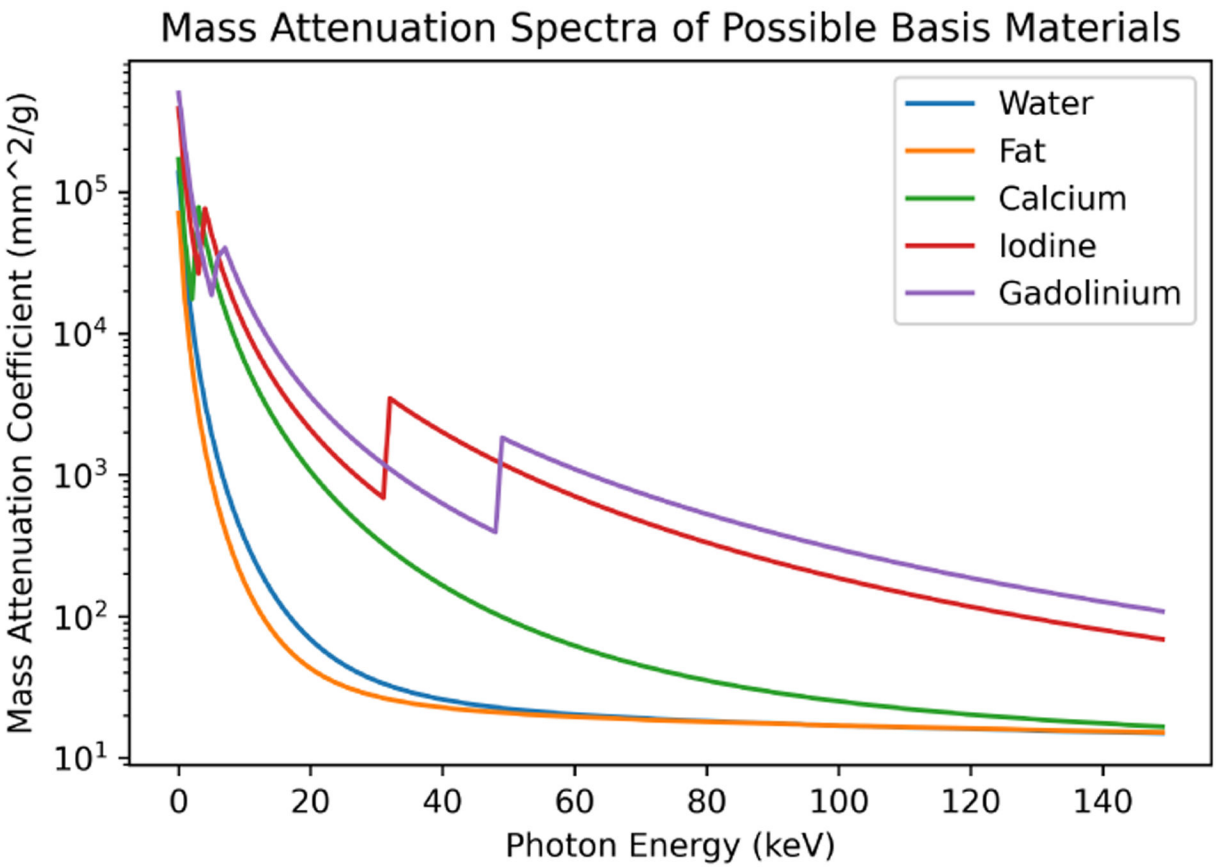

Fig. 14.
Mass attenuation spectra of possible basis materials.

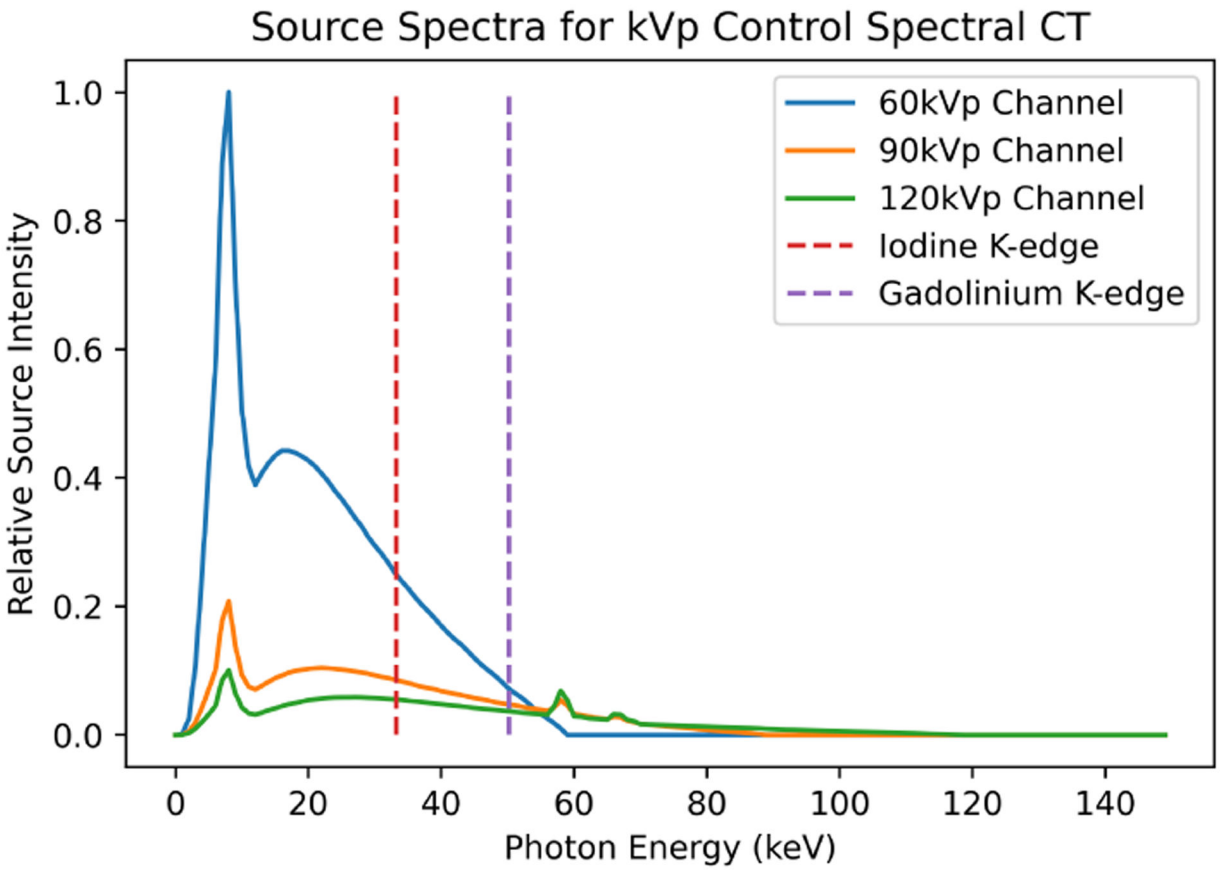

Fig. 15.
Source spectra for example kVp control system.

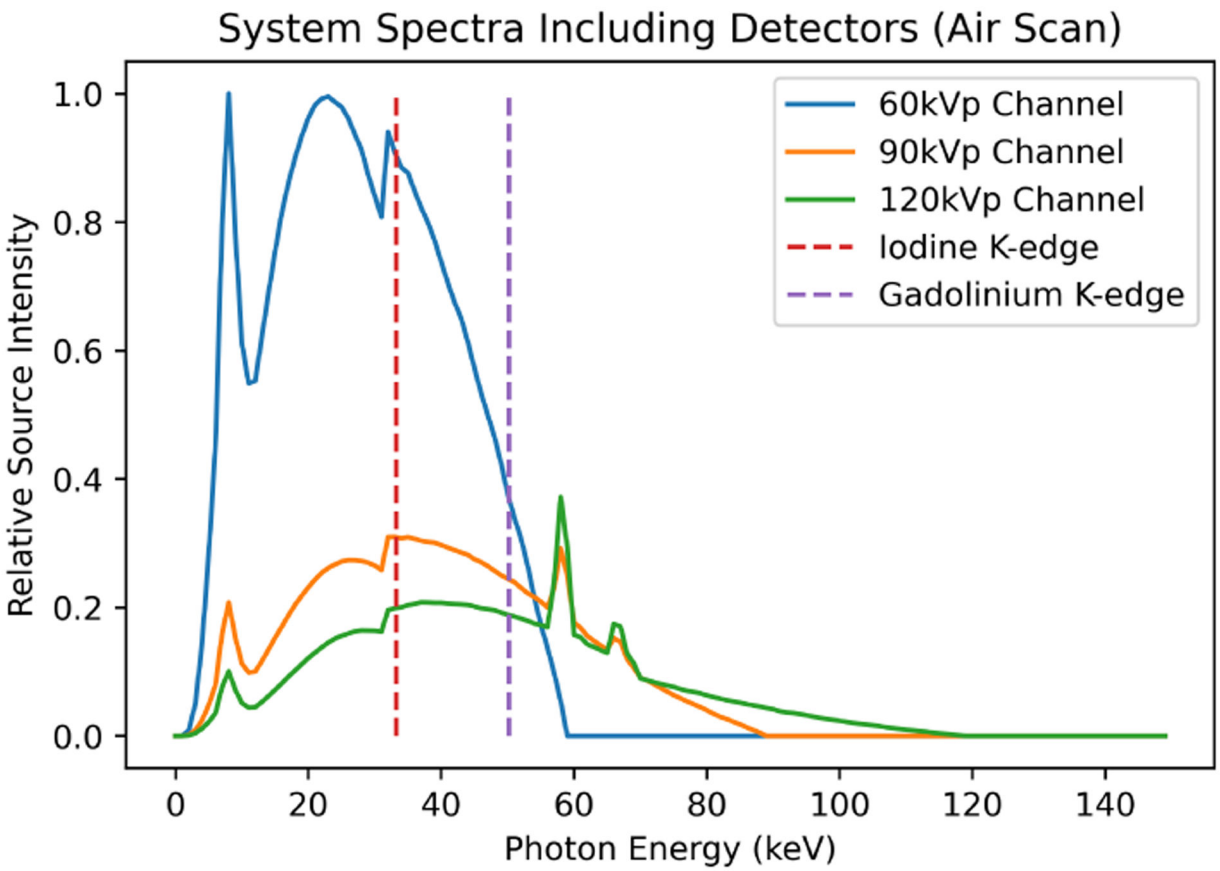

Fig. 16.
Total sensitivity spectra for example kVp control system.

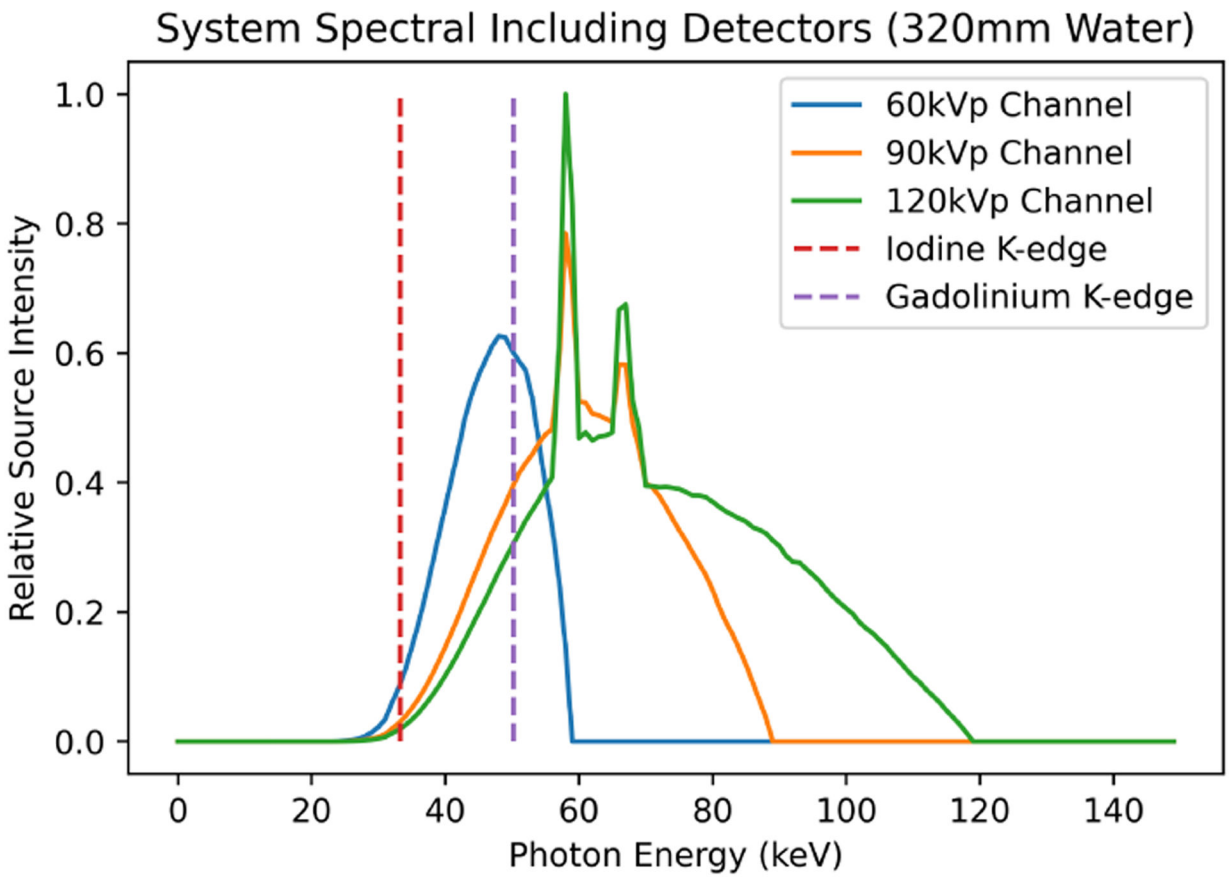

Fig. 17.

Total system sensitivity after attenuation from 320mm of water for example kVp control system.

TABLE I

Shapes And Other Properties Of The Matrix Operators In The Spectral CT Measurement Model

Matrix Operator	Shape
A	$(N_{\text{pixels}}\ N_{\text{materials}} \times N_{\text{voxels}}\ N_{\text{materials}})$
Q	$(N_{\text{pixels}}\ N_{\text{energies}} \times N_{\text{pixels}}\ N_{\text{materials}})$
S	$(N_{\text{pixels}}\ N_{\text{channels}} \times N_{\text{pixels}}\ N_{\text{energies}})$